https://doi.org/10.1016/j.compositesb.2016.09.022

Poly(ionic liquid)-Assisted Reduction of Graphene Oxide to Achieve High-Performance Composite Electrodes

Chengen He,[ad] Shan Sun,[a] Leping Huang,[b] Chi Pong Tsui,[c*] Xiaolin Xie,[d] and Yingkui Yang [ac*]

[a] *School of Materials Science and Engineering, Hubei University, Wuhan 430062, China*
E-mail: ykyang@hubu.edu.cn

[b] *School of Materials Science and Engineering, Wuhan Textile University, Wuhan 430200, China*

[c] *Department of Industrial and Systems Engineering, The Hong Kong Polytechnic University, Hung Hom, Kowloon, Hong Kong, China*
E-mail: gary.c.p.tsui@polyu.edu.hk

[d] *School of Chemistry and Chemical Engineering, Huazhong University of Science and Technology, Wuhan 430074, China*

Abstract

Direct reduction of graphene oxide (GO) to graphene often results in an irreversible agglomeration and hence suppressing its effective surface available for energy storage. In this work, GO was solvothermally reduced in the presence of imidazolium-based poly(ionic liquid) (PIL) of poly(1-butyl-3-vinylimidazolium hexafluorophosphate) to produce a PIL-modified reduced GO (PIL-rGO) composite. The integration of PILs with rGO is capable of preventing the restacking of rGO sheets, and hence, providing a large electrolyte ion-accessible surface and an abundant interior space for charge storage by enlarging the interlayer spacing in PIL-rGO. The PIL-rGO composite was then used as the supercapacitor electrode associated with a compatible IL of 1-butyl-3-methylimidazolium hexafluorophosphate as the electrolyte. The PIL herein improves the interface wettability between the electrode and electrolyte, and the IL electrolyte enables a wide potential window as well. Specific capacitances correspond to 196 F/g at a current density of 1 A/g, 160 F/g at 2 A/g, and 144.8 F/g at a scan rate of 60 mV/s, which are much higher than those (104 F/g at 2 A/g, and 48.1 F/g at 60 mV/s) of pure rGO. The capacitance retention is as high as 80.7% after 1000 charge-discharge cycles at a discharge current density of 2 A/g. The interfacial charge-transfer resistance of the PIL-rGO electrode (4.6 Ω) is also much lower than that of the rGO electrode (18.7 Ω). Such graphene-base electrodes may promise a candidate for high performance supercapacitors.

Keywords: Graphene; poly(ionic liquid)s; composite electrodes; supercapacitors

1. Introduction

Supercapacitors have attracted considerable attention in past two decades because of their attractive characteristics, such as their moderate energy density (~5 Wh/kg), long cycle life (>100,000), low maintenance costs, and, most importantly, high power density (>10 kW/kg, which is one order of magnitude larger than that of lithium-ion batteries) [1-3]. Additionally, they can be fully charged and discharged in a few seconds [4], and therefore, they have great potential for high-power applications, such as portable electronics, electric vehicles, and military equipment systems [4, 5]. Two general categories of supercapacitors exist: electric double-layer capacitors (EDLCs) and pseudocapacitors. EDLCs store energy through fast ion adsorption at the electrode surface, whereas pseudocapacitors storage energy by redox reactions between the electrode material and the electrolyte on/near the electrode surface. Generally, EDLCs enable higher power density but lower energy density compared to pseudocapacitors [6, 7]. To further improve the energy-storage performance, the specific surface area (SSA) of the electrode material must be increased to accommodate more ions at the electrode/electrolyte interface and, thus, enhance the EDL capacitance [1].

Carbon-based materials with high SSAs, such as carbon onions, carbon nanotubes, graphene, and activated carbon, are commonly used electrode materials in EDLCs [8]. Among these materials, graphene is the most promising because it has high electrical conductivity and a unique two-dimensional layer structure with exceptionally specific surface area (SSA, up to 2675 m^2/g) that could support an EDL capacitance value as high as 550 F/g if the SSA is fully utilized [9]. However, bulk graphene nanosheets tend to agglomerate and even restack to form graphite-like structures, thereby decreasing the effective SSA and specific capacitance [6, 10].

Therefore, the functionalization and interval of graphene nanosheets have become especially important for maximizing these materials' properties [11, 12]. Graphene-modification techniques include both covalent and noncovalent methods. The latter include polymer wrapping, the adsorption of surfactants or small aromatic molecules via Van der Waals forces, hydrogen bonding, electrostatic interactions, and/or π-π stacking. These methods seem to be more versatile and promising than the former because they do not affect graphene's lattice and, thus, its electronic properties are retained [13-16]. Modifying graphene also contributes to preventing the aggregation of graphene nanosheets and can be used to adjust their compatibilities with electrolytes, enhancing the electrolyte wettabilities and effective SSAs of graphene-based electrodes and thereby generating higher capacitances [17].

In addition to the electrode materials, the performance of supercapacitors is also strongly affected by the electrolytes employed [18]. Aqueous electrolytes have been widely utilized, but they have obvious drawbacks, which mainly include narrow cell potential windows and low energy densities. Organic electrolytes provide wider potential windows than aqueous electrolytes, but their low thermal stabilities and strong toxicities limit their use in supercapacitors [19]. Recently, ionic liquids (ILs, which are novel non-aqueous solvents composed of large organic cations and various anions) have attracted substantial attention because of their wide electrochemical windows, high ionic conductivities, excellent thermal and chemical stabilities, negligible vapor pressures, and low toxicities. Therefore, ILs are attractive electrolytes for high-performance supercapacitors [20, 21].

One major challenge is enhancing the IL ion accessibility of graphene-based electrodes. This improvement can be achieved by modifying the surface of the graphene sheets with ILs,

such as imidazolium ILs (Imi-ILs), which have surface tensions that closely match the surface energies of graphitic layers and interact non-covalently with the conjugated graphene surface through π-π and/or cation-π stacking. These interactions separate and structurally stabilize the graphene sheets, and thus, good wettability can be achieved with IL electrolytes [22]. Ramaprabhu et al. [22] reported an ultra-high-performance supercapacitor using a 1-butyl-3-methylimidazolium (BMI) bis(trifluoromethyl sulfonyl) imide-coated carbon nanotubes-graphene nanocomposite as the electrode and a hydrophobic IL as the electrolyte. This supercapacitor showed high specific capacitance (201 F/g) at a current density of 2 A/g and an extremely high energy density (171 Wh/kg) [23]. The authors believed that the improvement in the performance of the nanocomposite was mainly attributable to the presence of IL layers on the surface of the carbon nanomaterials, which effectively increased the electrolyte accessibility and decreased the lengths of the ion-transport paths.

In this study, we developed a one-pot method to non-covalently functionalize graphene through the solvothermal reduction of graphene oxide (GO) in the presence of poly(ILs) (PILs). PILs can be considered as a special type of polyelectrolyte containing repeating IL units in each polymer chain and combine the macromolecular architectures of polymers with the excellent electrochemical properties of ILs. The major advantages of PILs over ILs are their improved mechanical stabilities, processabilities, durabilities, and spatial controllabilities, and, hence, their novel functions and applications [24]. As expected, the prepared composites showed enhanced electrochemical performance, with high rate capabilities and excellent cycle performance.

2. Experimental

2.1. Materials

1-Butyl-3-vinylimidazolium hexafluorophosphate (BVI-PF_6) and BMI-PF_6 were obtained from Shanghai Chengjie Chemical Co., Ltd, and Henan Lihua Pharmaceutical Co., Ltd, respectively, and used as received. 1-Methyl-2-pyrrolidone (NMP) and azodiisobutyronitrile (AIBN) were purchased from Sinopharm Chemical Reagent Co., Ltd, and purified by reduced-pressure distillation and recrystallization, respectively. GO was prepared by a modified Hummers method, as described previously [25, 26].

2.2. Synthesis of PILs

PILs were prepared through the polymerization of unsaturated IL monomer salts. Specifically, poly(BVI) PF_6 (PBVI-PF_6) was synthesized via free radical polymerization as follows [27, 28]: BVI-PF6 (3.0 g, 10.1 mmol) was dissolved in 30 mL of NMP in a 100-mL round-bottom flask, and then, AIBN (0.01 g, 0.061 mmol) was added. The mixture was stirred and kept at 70°C under a nitrogen atmosphere for 3 h. Subsequently, the resulting precipitate was filtrated, washed several times with NMP, and dried at 80°C under vacuum for 12 h.

2.3. PIL-modified reduced GO (PIL-rGO)

PIL-rGO was produced by the simple solvothermal reduction of GO in the presence of a PIL. For this purpose, GO nanosheets and the PIL were suspended in NMP, and the suspension was then thermally treated at high temperature. During this process, the PIL likely becomes noncovalently functionalized on the surface of the graphene sheets, yielding PIL-rGO. Typically, 20 mg of GO powder was dispersed in 20 mL of anhydrous NMP with the aid of mild sonication. Then, 75 mg of a previously synthesized PIL was dissolved in this solution with stirring, forming a uniform, brown suspension. Next, the suspension was heated to 150°C for 1 h

in an oil bath and became black in color. After cooling, the suspension was filtered through a Teflon membrane (200-nm pore size) by vacuum filtration and washed with NMP to remove any excess PIL. Then, the obtained PIL-rGO was dried at 80°C in vacuum for 2 days. For comparison, solvothermally prepared rGO was also obtained without the PIL under comparable conditions.

2.4. Characterization

Transmission electron microscopy (TEM) was conducted using a Tecnai G220 electron microscope at 200 kV. Fourier transform infrared (FT-IR) spectra were recorded on a Spectrum One using KBr pellets. Thermogravimetric analysis (TGA) was performed using a PE TGA-7 calorimeter at a heating rate of 20°C/min in a nitrogen atmosphere. X-ray diffraction (XRD) experiments were conducted in a D/MAX-IIIC X-ray diffractometer with Cu K_{α} radiation. Raman spectra were collected with an excitation wavelength of 642.8 nm using a RFS-100/S Raman spectrometer.

The electrochemical performance was determined with a CHI 760E electrochemical workstation (Chenhua Instrument Company, Shanghai) in BMI-PF_6 electrolyte using a three-electrode system in which a platinum wire and a saturated calomel electrode (SCE) were used as the counter and reference electrodes, respectively. A PIL-rGO (or rGO) modified glassy carbon (GC) electrode was used as the working electrode and prepared by dropping 5 μL (1.0 mg/mL) of PIL-rGO (or rGO) dispersion onto a GC electrode (3-mm diameter) and drying it in an oven at 50°C for 1 h. Cyclic voltammetry (CV) was conducted at scan rates of 60~120 mV/s over a potential range of –1.0~2.0 V (vs. SCE). Galvanostatic charge-discharge (GCD) measurements were recorded at current densities of 1.0~6.0 A/g with the same voltage window.

Electrochemical impedance spectroscopy (EIS) was performed in a frequency range of 10,000 to 0.01 Hz with an alternating current (AC) amplitude of 10 mV.

3. Results and discussion

3.1. PIL-assisted reduction of GO

GO could be well dispersed in water and polar organic solvents, forming stable brown suspensions, because of the presence of oxygen-containing functional groups (OCFG) on the basal planes and edges of the GO nanosheets. These groups also make GO negatively charged, and thus, GO exhibits electrostatic interactions with the cations of PILs. Fig. 1 shows the process used to prepare the PIL-rGO. The addition of PIL to a suspension of GO in NMP typically yielded PIL-modified GO. This suspension was then heated at 150°C for 1 h to take advantage of the enhanced thermal deoxygenation at high temperatures and the chemical oxygen-scavenging ability of NMP [29], and the suspension turned black. This indicated that GO was solvothermally reduced to rGO and that PIL likely absorbed on the surface of the rGO sheets, yielding PIL-rGO.

GO could be exfoliated into few or even single-layer nanosheets using an ultrasonic dispersion method and stably dispersed in polar solvents, as shown in Fig. 2a. During the solvothermal-reduction process, deoxygenated GO formed a relatively regular graphitic structure, resulting in irreversibly agglomerated multilayer rGO microsheets with wrinkles in the layers (Fig. 2b) [29]. PIL-modified rGO produced a homogeneous colloidal system in NMP, and after being filtered and dried to obtain PIL-rGO power, it could be re-dispersed in other organic solvents, such as acetonitrile and dimethylformamide. As shown in Fig. 2c,d, PIL-rGO platelets

were observed as separated thin sheets with uniform PIL nanoparticles absorbed on the surface, which act as spacers to prevent the agglomeration of the rGO nanosheets.

Fig. 3a shows the FT-IR spectra of GO, PIL, and PIL-rGO. The spectrum of GO (Fig. 3a) showed peaks corresponding to O-H (3400 cm^{-1}), C=O (1722 cm^{-1}), aromatic C=C (1625 cm^{-1}), carboxy C-O (1387 cm^{-1}), epoxide/ether C-O (1213 cm^{-1}), and alkoxide C-O stretching (1051 cm^{-1}). However, the peak intensities of the oxygen-containing groups were decreased in the spectrum of PIL-rGO (Fig. 3c), indicating the de-oxygenation of GO after the solvothermal reduction [30]. Furthermore, peaks similar to those of pure PIL emerged at approximately 2850~3000; 1581, 1466, 1149, and 842; and 741 cm^{-1}, which were attributable to C-H, the aromatic rings of the Imi cation, and $-CH_2-CH_2-CH_2-CH_2-$ in the polymer main chain, respectively. These results indicated that rGO was successfully modified with PIL [31].

TGA was performed to qualitatively evaluate the degree of GO reduction and the PIL content in the PIL-rGO composite. Fig. 3b shows the TGA curves of GO, rGO, and PIL-rGO. GO showed a weight loss of 6.4% below 150°C, which was related to the removal of physisorbed water [17]. The significant weight loss of ~70.8% between 210 and 250°C resulted from the decomposition of oxygen-containing groups in the GO layer. In contrast, rGO showed much less weight loss than GO because of the elimination of oxygen-containing functional groups by the solvothermal reduction [32]. The weight loss of PIL-rGO below 250°C most likely corresponds to the removal of residual oxygen-containing groups, and the 16.5% weight loss between 250 and 550°C may be attributable to the co-decomposition of the coating PIL and the rGO framework [30]. Based on the weight losses exhibited by rGO and PIL in this temperature range (7.6% and 77.0%, respectively), the PIL content in PIL-rGO composite can

be roughly estimated to be 13%.

The XRD patterns of GO, rGO, and PIL-rGO are shown in Fig. 3c. GO exhibited an incisive diffraction peak at 2θ =10.9°, and the corresponding interlayer space was calculated to be 0.81 nm. A dispersing peak emerged at approximately 24.9° for rGO with a decreased interlayer space of 0.36 nm because of the removal of oxygen-containing groups from the basal plane [33]. Compared to that of rGO, the PIL-rGO diffraction peak intensity weakened and shifted to 20.6° with an interlayer space of 0.43 nm, indicating that PILs coated the surface of rGO sheets and acted as spacers, preventing the orderly stacking of the sheets [30].

Raman spectroscopy was employed to investigate the change in the conjugation state of the graphene plane. Fig. 3d shows the Raman spectra of GO, rGO, and PIL-rGO, which contained typical D (1341 cm^{-1}) and G (1589 cm^{-1}) bands indicating the presence of sp^3 defects and a sp^2 conjugated carbon network in the hexagonal plane, respectively [34]. Differences in the intensity ratios of the D band and G band (I_D/I_G) suggest that the defects present in the graphene structure changed. The I_D/I_G value of rGO (1.10) was higher than that of GO (0.97), indicating the existence of more defects because of the edge effect caused by the relatively small average size of the rGO sheets [35]. For PIL-rGO, the I_D/I_G was 1.03, which is lower than that of rGO and shows that PIL-rGO contains fewer defects than rGO.

3.2. Electrochemical performance of PIL-rGO

The electrochemical performance of the PIL-rGO-based electrode was analyzed using BMI-PF_6 as the electrolyte in a classic three-electrode system. The electrolyte was purged with pure nitrogen for 15 min prior to the measurements, which could be performed under ambient

conditions because of the hydrophobic nature of BMI-PF_6 [36]. The CV curves of the PIL-rGO electrode obtained using scan rates of 60, 80, 100, and 120 mV/s are shown in Fig. 4a. These CV curves are nearly rectangular in shape, even at the highest scan rate tested (120 mV/s), indicating that, in the composite electrode, the charge storage mainly occurs via the EDLC mechanism, However, the presence of the functional groups on the surface of the rGO sheets likely contributed a small amount of pseudocapacitance [37].

The C_S was calculated by integrating the areas under the CV curves according to the following equation [38, 39]: $C_S = \frac{\int \frac{i}{m} dV}{\Delta V v}$

where i/m represents the current density (A/g), v is the scan rate (mV/s), and ΔV is the potential window (V). The C_S values of the PIL-rGO-based electrode correspond to capacitances as high as 144.8 F/g at the low scan rate of 60 mV/s; this value is three times higher than that of the pure rGO-based electrode (48.1 F/g) (Fig. 4b). Even at a high scan rate of 120 mV/s, PIL-rGO still displayed a capacitance of 136.0 F/g with a *C*s retention of 93.9%, implying excellent rate performance and the capability of fast charge-discharge. The excellent performance of PIL-rGO may be attributed to the presence of PIL adsorbed on the surface of the rGO sheets, preventing them from aggregating. In addition, the similarity and miscibility of PIL and BMI-PF_6 enhance the electrolyte accessibility by effectively increasing the number of ion-diffusion paths inside the electrode and thereby improving the effective SSA of the composite [40].

The GCD curves of PIL-rGO at current densities of 1, 2, 4, and 6 A/g are shown in Fig. 5a. All of the curves have similar shapes, indicating that the PIL-rGO composite has a relatively

high ion conductivity that can sustain fast ion diffusion between the electrodes and the electrolyte [17]. The specific capacitances were calculated from the discharge data according to the following Equation:

$$C_s = \frac{i\,\Delta t}{\Delta V m}$$

where i is the applied current (A), Δt is the discharge time (s), ΔV is the potential change during the discharge process, and m is the mass of the active material on the GC electrode. The specific capacitances of the PIL-rGO-based electrode were calculated to be 196, 160, 140, and 112 F/g at current densities of 1, 2, 4, and 6 A/g, respectively, whereas the rGO-based electrode had a capacitance of only 104 F/g at 2 A/g (Fig. 5b). This remarkable enhancement is consistent with these electrodes' CV curves. Modifying graphene with PIL increased the surface/interface accessible to the electrolyte and facilitated the utilization of the electrode's whole SSA, resulting in a higher specific capacitance. Additionally, the PIL on the graphene surface allowed the fast transportation of ions through the electrode, resulting in excellent rate capability.

EIS was employed to evaluate the electrodes' resistance characteristics. Fig. 6a shows the Nyquist plots of rGO and PIL-rGO composite electrodes. Each curve contains a clear semicircle in the high-frequency region, a ~45° inclined line in the midfrequency region, and a nearly vertical line in the low frequency region; these features are characteristic of capacitive behavior [41]. The impedance spectra were then analyzed using the complex nonlinear least-squares fitting method according to the equivalent circuit, as shown in Fig. 6b. The intercept of the real axis in the high-frequency region corresponds to the contact resistance (R_{ES}). Both the rGO and PIL-rGO composite electrodes exhibited similar contact resistances of ~ 5 Ω. The diameter of the semicircle

reflects the interfacial charge-transfer resistance (R_{CT}) caused by Faradaic reactions and EDLC (C_{DL}) on the grain surface of the active materials [42]. The R_{CT} value of the PIL-rGO electrode (4.6 Ω) was much lower than that of the rGO electrode (18.7 Ω), possible because of the repeating IL units in the polymer chains of the PIL, which can decrease the interfacial resistance between the electrode and electrolyte. The inclined portion (~45°) is typically represented by the Warburg resistance (Z_W), which corresponds to ion diffusion and transport from the electrolyte into the electrode. The PIL-rGO-based electrode had a significantly shorter Warburg region than the rGO-based one, suggesting faster ion diffusion and transport within the PIL-rGO electrode because of the enhanced compatibility between the PIL-rGO composite and the IL electrolyte [43]. The nearly vertical portion in the low-frequency region was extrapolated to the real axis to represent the total equivalent series resistance (ESR) of the electrode, and the total ESR of the PIL-rGO-based electrode was estimated to be 12.6 Ω, which is much lower than that of the rGO-based electrode (31.3 Ω). These values are much higher than those recorded for some aqueous electrolyte-based supercapacitors because of IL electrolytes' lower electrical conductivities and higher viscosities. Thus, the negative impact of the IL electrolyte's lower ionic conductivity may be offset by the increase in the operating voltage required to achieve high energy and power densities [44, 45].

The cycle life of a supercapacitor is one of the most important factors for practical applications, and the electrochemical stability of PIL-rGO was examined by GCD at a current density of 2 A/g for 1000 cycles. As shown in Fig. 7, the initial specific capacitance of the PIL-rGO electrode was 160 F/g, and after 1000 cycles, it plateaued at approximately 129 F/g,

corresponding to a decrease of 19.3%. Achieving excellent cyclic stability depends on the electrochemical stability of the electrode material and electrolyte [46]. This finding clearly suggests that no noteworthy irreversible electrochemical reaction occurs between the PIL-rGO electrode and the electrolyte because of their good electrochemical stabilities [22].

4. Conclusions

This work characterizes a noncovalently PIL-modified rGO composite obtained through a one-pot solvothermal reduction process. An electrode based on this composite was tested in a compatible IL electrolyte over a wide potential window of 3 V, and a high specific capacitance (over 196 F/g) was recorded at a current density of 1 A/g. This electrode also exhibited remarkably enhanced capacitive performance compared to that of pure rGO because of the presence of PIL, which prevents the aggregation of the rGO sheets and improves the composite's IL wettability. These effects synergistically enhanced the effective SSA of the PIL-rGO electrode. The PIL-rGO electrode also achieved a long cycle life with 80.7% retention of the initial capacitance after 1000 charge-discharge cycles at 2 A/g. This promising material is expected to be utilized for the fabrication of high-performance supercapacitors.

Acknowledgements

We thank the financial support from the National Natural Science Foundation of China (51273057), the Program for New Century Excellent Talents in University (NCET-12-0709), the Funds for Distinguished Young Scientists in Hubei (2015CFA048), the Research Committee of the Hong Kong Polytechnic University (Project code: G-UC81), and the Chutian Scholar Program of Hubei Province (China).

References

[1] Yan J, Wang Q, Wei T, Fan ZJ. Recent advances in design and fabrication of electrochemical supercapacitors with high energy densities. Adv Energy Mater 2014;4(4):1300816.
[2] Simon P, Gogotsi Y. Materials for electrochemical capacitors. Nat Mater 2008;7(11):845-54.
[3] Yang YK, Han CP, Jiang BB, Iocozzia J, He CE, Shi DA, et al. Graphene-based materials with tailored nanostructures for energy conversion and storage. Mater Sci Eng, R 2016;102:1-72.
[4] Zhai Y, Dou Y, Zhao D, Fulvio PF, Mayes RT, Dai S. Carbon materials for chemical capacitive energy storage. Adv Mater 2011;23(42):4828-50.
[5] Cheng Q, Tang J, Ma J, Zhang H, Shinya N, Qin LC. Graphene and carbon nanotube composite electrodes for supercapacitors with ultra-high energy density. Phys Chem Chem Phys 2011;13(39):17615-24.
[6] Huang Y, Liang J, Chen Y. An overview of the applications of graphene-based materials in supercapacitors. Small 2012;8(12):1805-34.
[7] Wang GP, Zhang L, Zhang JJ. A review of electrode materials for electrochemical supercapacitors. Chem Soc Rev 2012;41(2):797-828.
[8] Simon P, Gogotsi Y. Capacitive energy storage in nanostructured carbon electrolyte systems. Acc Chem Res 2013;46(5):1094-103.
[9] Liu CG, Yu ZN, Neff D, Zhamu A, Jang BZ. Graphene-based supercapacitor with an ultrahigh energy density. Nano Lett 2010;10(12):4863-8.
[10] Sun Y, Wu Q, Shi G. Graphene based new energy materials. Energy Environ Sci 2011;4(4):1113-32.
[11] Seredych M, Hulicova-Jurcakova D, Lu GQ, Bandosz TJ. Surface functional groups of carbons and the effects of their chemical character, density and accessibility to ions on electrochemical performance. Carbon 2008;46(11):1475-88.
[12] Dai L. Functionalization of graphene for efficient energy conversion and storage. Acc Chem Res 2013;46(1):31-42.
[13] An XH, Simmons TJ, Shah R, Wolfe C, Lewis KM, Washington M, et al. Stable aqueous dispersions of noncovalently functionalized graphene from graphite and their multifunctional high-performance applications. Nano Lett 2010;10(11):4295-301.
[14] Liu J, Tang J, Gooding JJ. Strategies for chemical modification of graphene and applications of chemically modified graphene. J Mater Chem 2012;22(25):12435-52.
[15] Mann JA, Dichtel WR. Noncovalent functionalization of graphene by molecular and polymeric adsorbates. J Phys Chem Lett 2013;4(16):2649-57.
[16] Georgakilas V, Otyepka M, Bourlinos AB, Chandra V, Kim N, Kemp KC, et al. Functionalization of graphene: covalent and non-covalent approaches, derivatives and applications. Chem Rev 2012;112(11):6156-214.
[17] Trigueiro JPC, Lavall RL, Silva GG. Supercapacitors based on modified graphene electrodes with poly(ionic liquid). J Power Sources 2014;256:264-73.
[18] Zhang LL, Zhao XS. Carbon-based materials as supercapacitor electrodes. Chem Soc Rev 2009;38(9):2520-31.
[19] Zhong C, Deng Y, Hu W, Qiao J, Zhang L, Zhang J. A review of electrolyte materials and compositions for electrochemical supercapacitors. Chem Soc Rev 2015;44(21):7484-539.

[20] Shao QG, Tang J, Lin YX, Li J, Qin FX, Yuan JS, et al. Carbon nanotube spaced graphene aerogels with enhanced capacitance in aqueous and ionic liquid electrolytes. J Power Sources 2015;278:751-9.
[21] Sun Y, Cheng Y, He K, Zhou A, Duan H. One-step synthesis of three-dimensional porous ionic liquid-carbon nanotube-graphene gel and MnO_2-graphene gel as freestanding electrodes for asymmetric supercapacitors. RSC Adv 2015;5(14):10178-86.
[22] Kim J, Kim S. Preparation and electrochemical property of ionic liquid-attached graphene nanosheets for an application of supercapacitor electrode. Electrochim Acta 2014;119:11-5.
[23] Tamailarasan P, Ramaprabhu S. Carbon nanotubes-graphene-solidlike ionic liquid layer-based hybrid electrode material for high performance supercapacitor. J Phys Chem C 2012;116(27):14179-87.
[24] Peng RG, Wang YZ, Tang W, Yang YK, Xie XL. Progress in imidazolium ionic liquids assisted fabrication of carbon nanotube and graphene polymer composites. Polymers 2013;5(2):847-72.
[25] Yang YK, He CE, Tang W, Tsui CP, Shi D, Sun ZG, et al. Judicious selection of bifunctional molecules to chemically modify graphene for improving nanomechanical and thermal properties of polymer composites. J Mater Chem A 2014;2(47):20038-47.
[26] Yang YK, Zhan WJ, Peng RG, He CE, Pang XC, Shi D, et al. Graphene-enabled superior and tunable photomechanical actuation in liquid crystalline elastomer nanocomposites. Adv Mater 2015;27(41):6376-81.
[27] Marcilla R, Alberto Blazquez J, Rodriguez J, Pomposo JA, Mecerreyes D. Tuning the solubility of polymerized ionic liquids by simple anion-exchange reactions. J Polym Sci, Part A: Polym Chem 2004;42(1):208-12.
[28] Kim TY, Lee TH, Kim JE, Kasi RM, Sung CS, Suh KS. Organic solvent dispersion of poly (3, 4-ethylenedioxythiophene) with the use of polymeric ionic liquid. J Polym Sci, Part A: Polym Chem 2008;46(20):6872-9.
[29] Dubin S, Gilje S, Wang K, Tung VC, Cha K, Hall AS, et al. A one-step, solvothermal reduction method for producing reduced graphene oxide dispersions in organic solvents. ACS Nano 2010;4(7):3845-52.
[30] Tung TT, Kim TY, Shim JP, Yang WS, Kim H, Suh KS. Poly(ionic liquid)-stabilized graphene sheets and their hybrid with poly(3,4-ethylenedioxythiophene). Org Electron 2011;12(12):2215-24.
[31] Gurban AM, Rotariu L, Baibarac M, Baltog I, Bala C. Sensitive detection of endocrine disrupters using ionic liquid--single walled carbon nanotubes modified screen-printed based biosensors. Talanta 2011;85(4):2007-13.
[32] Becerril HA, Mao J, Liu Z, Stoltenberg RM, Bao Z, Chen Y. Evaluation of solution-processed reduced graphene oxide films as transparent conductors. ACS Nano 2008;2(3):463-70.
[33] Mhamane D, Ramadan W, Fawzy M, Rana A, Dubey M, Rode C, et al. From graphite oxide to highly water dispersible functionalized graphene by single step plant extract-induced deoxygenation. Green Chem 2011;13(8):1990-6.
[34] Kudin KN, Ozbas B, Schniepp HC, Prud'homme RK, Aksay IA, Car R. Raman spectra of graphite oxide and functionalized graphene sheets. Nano Lett 2008;8(1):36-41.
[35] Tang LC, Wan YJ, Yan D, Pei YB, Zhao L, Li YB, et al. The effect of graphene dispersion

on the mechanical properties of graphene/epoxy composites. Carbon 2013;60:16-27.
[36] Schröder U, Wadhawan JD, Compton RG, Marken F, Suarez PAZ, Consorti CS, et al. Water-induced accelerated ion diffusion: voltammetric studies in 1-methyl-3-[2,6-(S)-dimethylocten-2-yl]imidazolium tetrafluoroborate, 1-butyl-3-methylimidazolium tetrafluoroborate and hexafluorophosphate ionic liquids. New J Chem 2000;24(12):1009-15.
[37] Kim TY, Lee HW, Stoller M, Dreyer DR, Bielawski CW, Ruoff RS, et al. High-performance supercapacitors based on poly(ionic liquid)-modified graphene electrodes. ACS Nano 2011;5(1):436-42.
[38] Xu CH, Xu BH, Gu Y, Xiong ZG, Sun J, Zhao XS. Graphene-based electrodes for electrochemical energy storage. Energy Environ Sci 2013;6(5):1388-414.
[39] Dai YM, Tang SC, Vongehr S, Meng XK. Silver nanoparticle-induced growth of nanowire-covered porous MnO_2 spheres with superior supercapacitance. ACS Sustainable Chem Eng 2014;2(4):692-8.
[40] Fu C, Kuang Y, Huang Z, Wang X, Yin Y, Chen J, et al. Supercapacitor based on graphene and ionic liquid electrolyte. J Solid State Electrochem 2010;15(11-12):2581-5.
[41] Zhu C, Zhai J, Wen D, Dong S. Graphene oxide/polypyrrole nanocomposites: one-step electrochemical doping, coating and synergistic effect for energy storage. J Mater Chem 2012;22(13):6300-6.
[42] Jeong GH, Lee HM, Lee HW, Kim CK, Piao YZ, Lee JH, et al. One-pot synthesis of thin $Co(OH)_2$ nanosheets on graphene and their high activity as a capacitor electrode. RSC Adv 2014;4(93):51619-23.
[43] Lei ZB, Liu ZH, Wang HJ, Sun XX, Lu L, Zhao XS. A high-energy-density supercapacitor with graphene-CMK-5 as the electrode and ionic liquid as the electrolyte. J Mater Chem A 2013;1(6):2313-21.
[44] Chen Y, Zhang XO, Zhang DC, Yu P, Ma YW. High performance supercapacitors based on reduced graphene oxide in aqueous and ionic liquid electrolytes. Carbon 2011;49(2):573-80.
[45] Van Aken KL, Beidaghi M, Gogotsi Y. Formulation of ionic-liquid electrolyte to expand the voltage window of supercapacitors. Angew Chem Int Ed Engl 2015;54(16):4806-9.
[46] Tamilarasan P, Ramaprabhu S. Nitrogen-doped graphene for ionic liquid based supercapacitors. J Nanosci Nanotechnol 2015;15(2):1154-61.

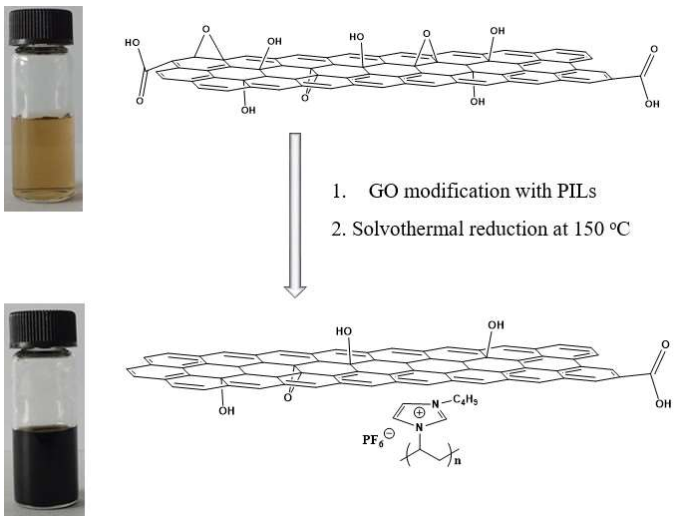

Fig. 1. The process used to prepare PIL-rGO.

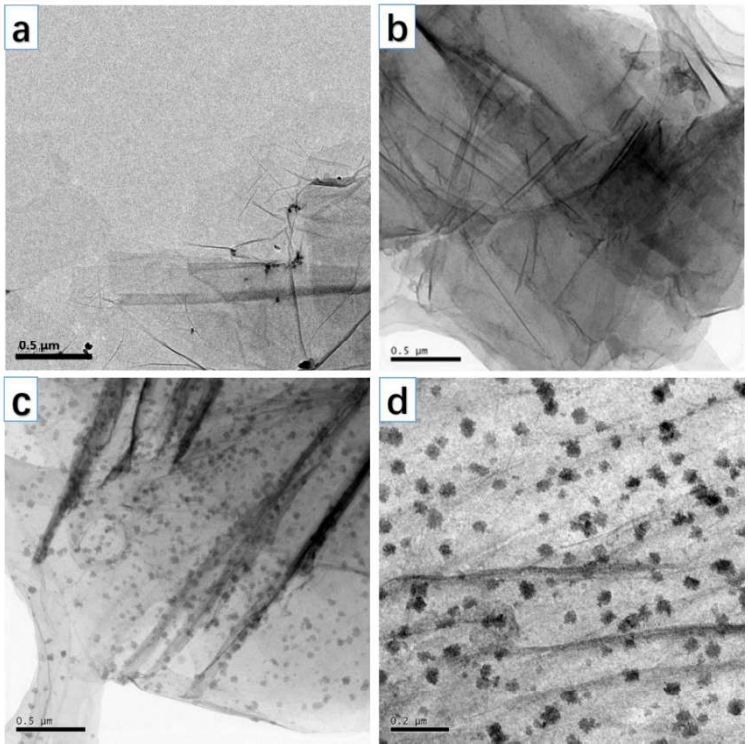

Fig. 2. TEM images of GO (a), rGO (b), and PIL-rGO (c,d).

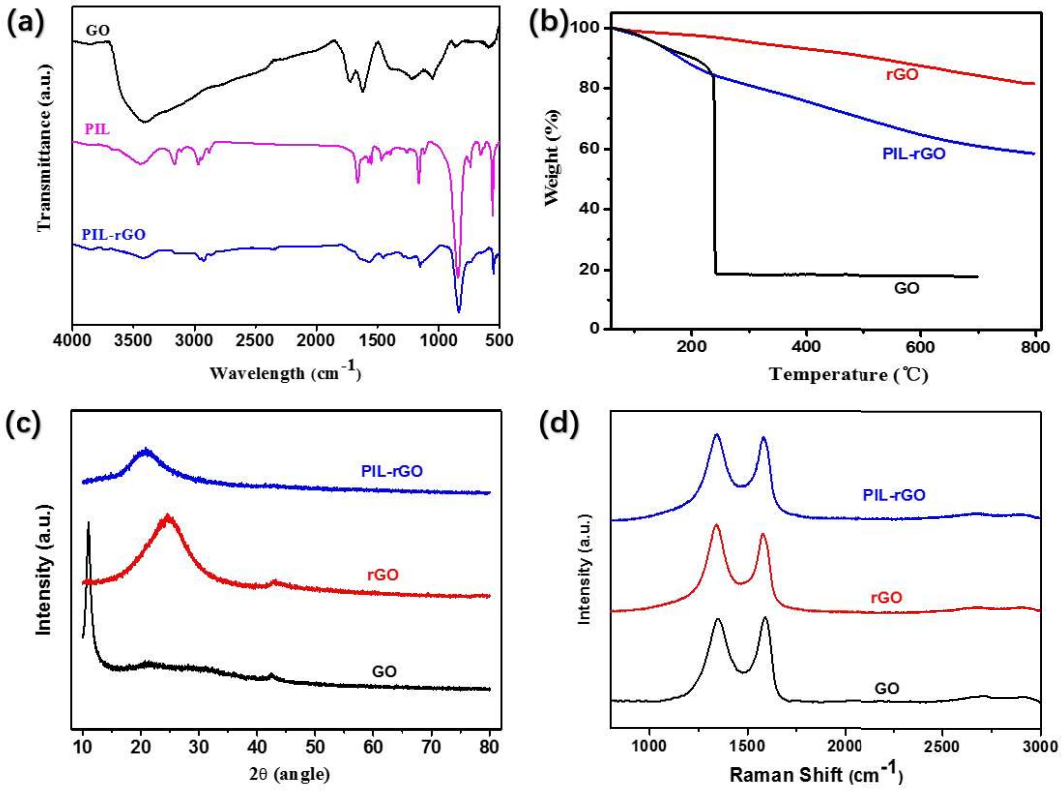

Fig. 3. (a) FTIR, (b) TGA, (c) XRD, and (d) Raman results of GO (black), PIL (pink), rGO (red), and PIL-rGO (blue).

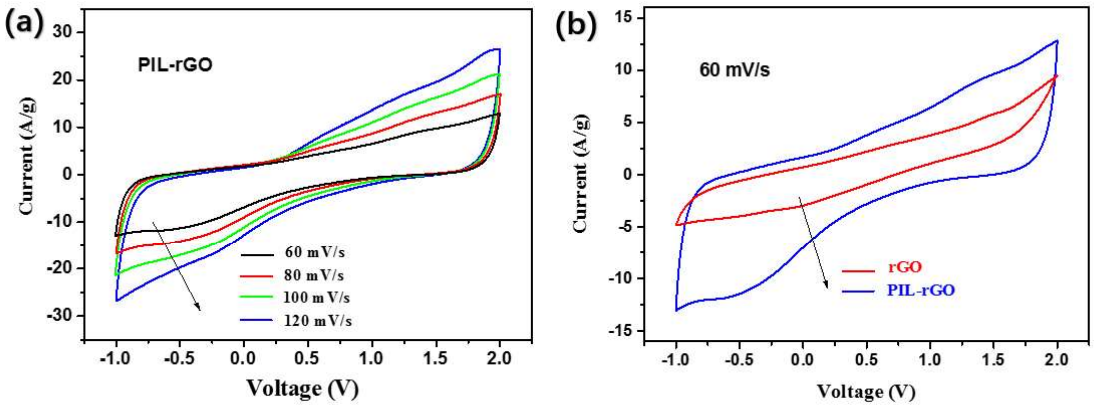

Fig. 4. (a) FTIR, (b) TGA, (c) XRD, and (d) Raman results of GO (black), PIL (pink), rGO (red), and PIL-rGO (blue).

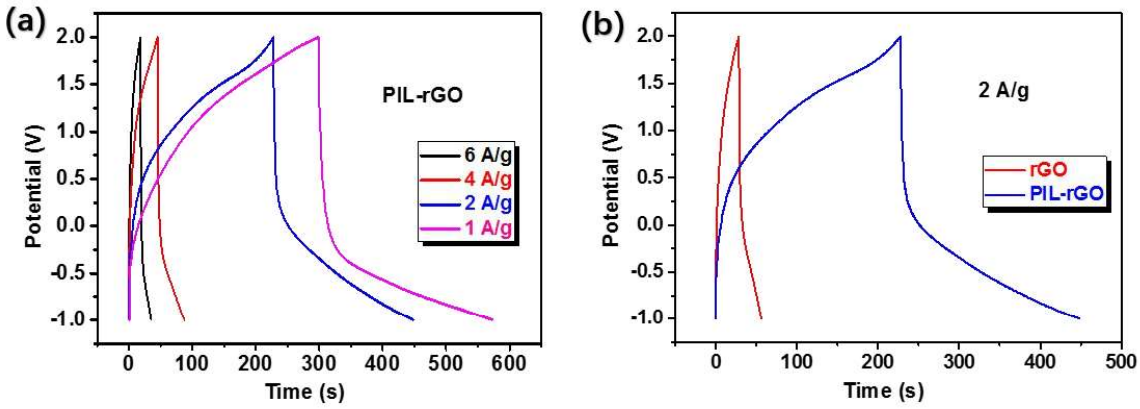

Fig. 5. GCD curves of (a) PIL-rGO at different constant currents and (b) rGO *vs* PIL-rGO at a current density of 2 A/g.

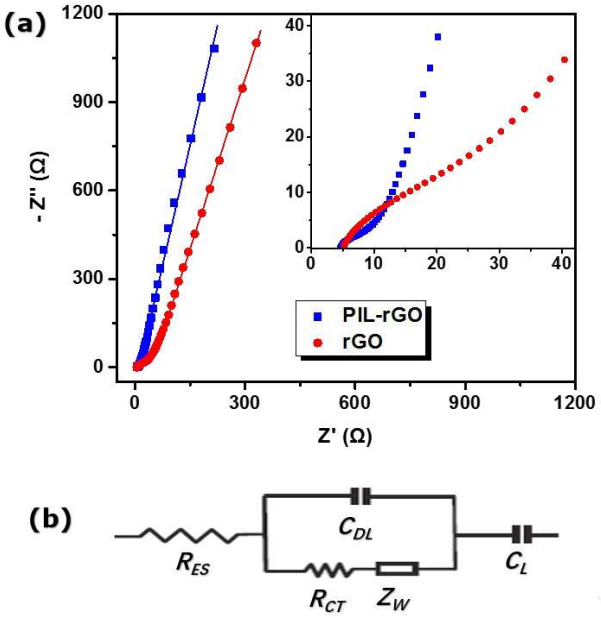

Fig. 6. (a) Nyquist plots of rGO and PIL-rGO composite and (b) the electrical equivalent circuit used for fitting the impedance spectra.

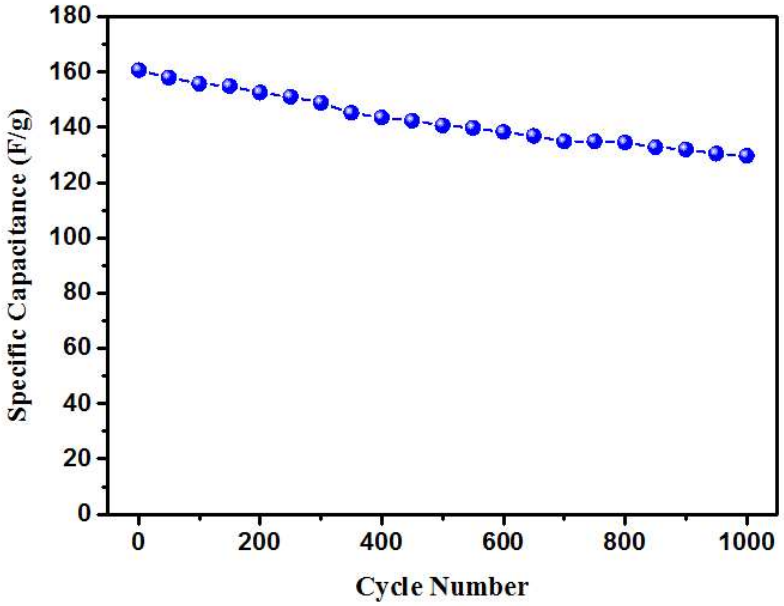

Fig. 7. Cycling performance of PIL-rGO.